旋转电弧传感器特征谐波法的改进

李志刚， 张 华， 高延峰
（南昌大学 江西省机器人与焊接自动化重点实验室，南昌 330031）

摘 要：利用特征谐波检测法进行焊缝偏差的检测是旋转电弧传感器焊缝偏差检测方法之一. 通过在焊接倾角存在情况下对特征谐波法的数学分析和模拟仿真，深入探讨了特征谐波中焊缝偏差、焊缝倾角和初始相位、跟踪调整的相位角的关系，对特征谐波方法进行了改进，证明了特征谐波方法结果中的实部和虚部可以分别用来对焊缝偏差和焊枪倾角检测. 并且在只对焊缝偏差检测情况下，采用特征谐波方法结果中的实部表征特征量比采用其幅值效果好. 结果表明，这种方法对偏差检测的效果比传统的特征谐波方法抗干扰能力更强.

关键词：旋转电弧传感器；偏差检测；特征谐波
中图分类号：TG409 文献标识码：A 文章编号：0253－360X(2009)05－0053－04

李志刚

0 序 言

旋转电弧传感器扫描焊炬位置高度变化得到焊接电流的变化. 旋转电弧传感系统的优点是抗弧光、高温和强磁场能力强，传感器和焊接电弧合一，没有位置和时间的差别. 其弱点是抗电流干扰能力差.

1996 年潘际銮院士、吴世德利用计算机仿真，首次提出基于特征谐波的变换空间方法，通过分析得到不同坡口扫描输入信号的特征谐波（特征谐波就是反映坡口偏差状态的谐波），指出特征谐波分量的大小和相位这两个特征分量可以反应坡口偏差[1－5]. 实践证明这种方法可以进行焊枪偏差检测，但是这种方法也存在一定的缺陷，在焊缝偏差为 0 的附近，往往检测效果很差，文章通过对特征谐波检测方法的改进，深入研究了特征谐波中焊缝偏差、焊缝倾角和初始相位、跟踪调整的相位角的关系. 分析了在焊缝偏差为 0 的附近检测效果差的根本原因，对这种方法进行了改进，通过水淹旋转电弧传感器气罩条件下的试验证实了这种方法的优越性.

1 焊缝偏差与倾角及弧长对应关系

不存在焊炬倾角的情况下，焊炬高度的变化为

$$H(t) = H_0 - |R\sin\omega t - e|\tan\alpha \qquad (1)$$

式中：H_0 为焊炬高度；R 为电弧旋转半径；ω 为顺时针旋转角速度；α 为坡口与水平面的夹角；e 为电弧旋转中心与焊缝偏移量.

在实际焊接过程中，存在着焊炬倾角，这种情况下，焊炬高度变化的表达式就不成立了.

定义焊炬轴线与垂直线的夹角称为倾角，沿着焊接的方向，焊炬上端超前于末端的情形称为后倾，反之称为前倾，如图 1 所示的焊接状态为后倾.

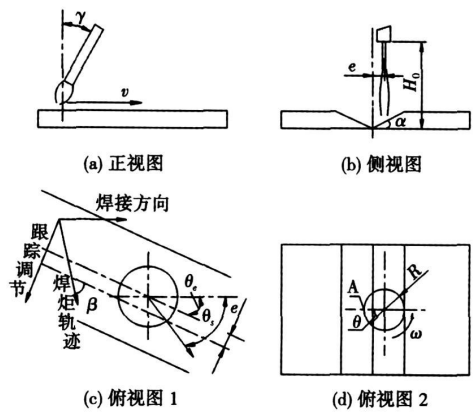

图 1 焊炬与焊件相对位置

Fig. 1 Position of welding torch comparing with weldment

设 A 点开始，经过任意时刻 t，焊炬高度的变化为[6]

收稿日期：2008－11－18
基金项目：国家 863 高技术研究发展计划资助项目（2007AA04Z242）；
江西省科技厅工业攻关项目（2007BG09200）

$$H(t) = H_0 - R\sin(\omega t + \beta) \cdot \sin\gamma - |e - R\cos(\omega t + \beta)|\tan\alpha \quad (2)$$

式中：β 为焊炬轨迹与焊接方向夹角；γ 为电弧旋转面的倾角.

2 带焊炬倾角的特征谐波法

根据理论研究和试验结果可知，电源 — 电弧传感系统可以简化成一个线性系统 $I(s) = G(s)H(s)$，其中 $G(s)$ 是系统的传递函数. 根据线性系统的叠加性质，传感电流信号是输入信号（扫描焊炬高度变化）的各次谐波激励单独作用所产生的响应之和[1].

因此输入的焊炬高度变化唯一确定了电流输出信号，对于 V 形坡口，电流传感信号的一次谐波幅值与偏差有线性关系. 由一次谐波的幅值即可检测焊缝偏差 e. 这里的一次谐波就是特征谐波，这种检测焊缝偏差的方法即为特征谐波检测法. 对式(1)作傅立叶变换，得一次谐波，其幅值为

$$a_1 = \frac{R\tan\alpha(2\theta + \sin\theta)}{\pi} \quad (3)$$

式中：$\theta = \arcsin(\frac{e}{R})$.

对于有焊炬倾角的情况，如果还是用电流传感信号的一次谐波来判断焊缝偏差，将会出现很大的误差. 因为通过对 $H(t)$ 进行傅立叶变换的一次谐波的实部和虚部分别为

$$\left.\begin{aligned} a_1 &= \frac{R\pi\sin\beta\sin\gamma + R\tan\alpha(2\theta\cos\beta + \sin 2\theta)}{\pi} \\ b_1 &= \frac{R\pi\cos\beta\sin\gamma - R\tan\alpha(2\theta\sin\beta + \sin\beta\sin 2\theta)}{\pi} \end{aligned}\right\} \quad (4)$$

从中可以看出 a_1，b_1 受 β 的影响. 而焊炬轨迹与焊接方向夹角 β 受到两个因素的影响，一个是焊缝与焊接方向存在的夹角 θ_e，一个是跟踪时焊炬要进行不停的左右调整，使得焊炬运动方向与焊缝存在一个变动的角度 β'. 实际跟踪时 θ_e 和 β' 合为一个 β. 同时由于系统传递函数的存在，特征谐波分量也会产生相位移动 θ_s. 因此闭环时，实际的坡口扫描信号特征谐波向量的初始相位只受到 θ_s，β 的影响，此时

$$\theta_0 = \theta_s + \beta \quad (5)$$

这样向量变化如图 2 所示.

$$a_{e+\gamma} \cdot e^{j\beta} \rightarrow G(S) \rightarrow A_{e+\gamma} \cdot e^{j\theta_0}$$

图 2 特征谐波分量变化

Fig. 2 Changing of characteristic harmonic

因此坡口扫描信号中特征谐波幅值 $a_{e+\gamma}$ 经过系统传输后为 $A_{e+\gamma}$，此时的幅值不再单独反映坡口偏差的变化，同时还有焊炬倾角变化反映在里面，所以这种情况下用 $A_{e+\gamma}$ 来单独检测焊缝偏差就不准确了. 同时，系统传输后相位也发生了变化，由 β 改变为 θ_0，θ_0 对坡口偏差和焊炬倾角的检测影响也是不能忽略的.

当 β 为 0 时，式(4)简化为

$$\left.\begin{aligned} a_1 &= \frac{R\tan\alpha(2\theta + \sin 2\theta)}{\pi} \\ b_1 &= R\sin\gamma \end{aligned}\right\} \quad (6)$$

从中可以得出 β 为 0 时，a_1 只受到坡口偏差的影响，偏差取值由 −3 ~ +3，间隔 0.5，对应图 3 中偏差变化 1 ~ 13 次，此时 Matlab 仿真图形如图 3 所示.

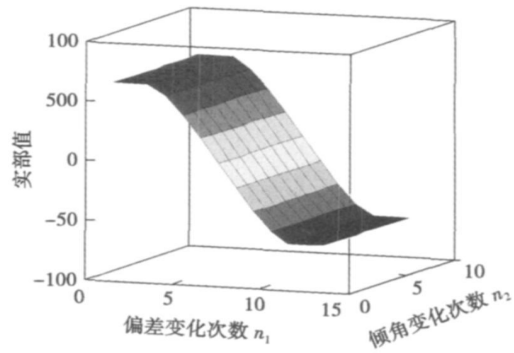

图 3 偏差变化与特征谐波实部的关系

Fig. 3 Relationship between deviation change and real part of characteristic harmonic

b_1 只受到焊炬倾角的影响，焊炬倾角由 −π/4 ~ π/4，变化间隔 π/32，对应图 3 中倾角变化 1 ~ 17 次，此时 Matlab 仿真图形如图 4 所示.

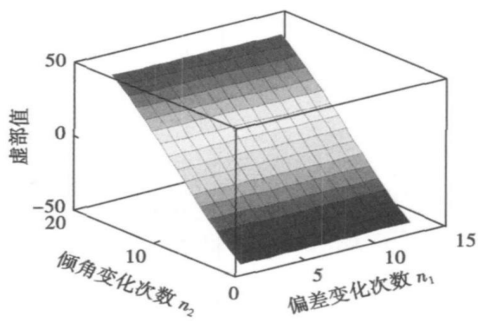

图 4 倾角变化与特征谐波虚部的关系

Fig. 4 Relationship between obliquity change and imagnary part of characteristic harmonic

大多数焊接过程中，倾角和 β 是同时存在的，

但倾角往往在某一固定值附近，这时可以发现在偏差范围为 0 附近时，用幅值法判断偏差，随倾角的不同，幅值会有很大的不同，如图 5 所示，用 Matlab 仿真倾角为 π/6，β 由 −π/6 变到 π/6，每次变化量为 π/12，偏差由 −3 变化取值到 3，间隔 0.5 时的幅值变化情况，当 β 为[π/6, 0] 时，[0, 0.5] 偏差处的幅值偏向偏差范围为正的区域，当 β 为[π/12, π/6] 时，[−0.5, 0] 偏差处的幅值范围为负的区域，而此时的偏差都应该为 0 附近，这样就造成了误判．这是用幅值法无法很好地检测到偏差为 0 的情况的根本原因．

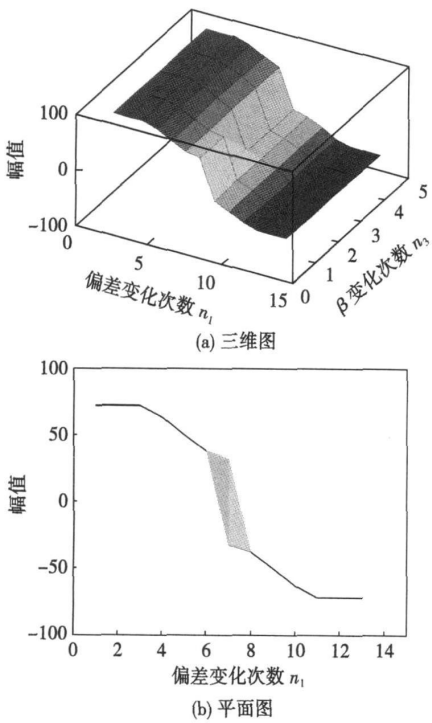

图 5　β 与幅值的关系

Fig. 5　Relationship between β change and amplitude

当 β 不为 0 时，a_1 和 b_1 同时受偏差和倾角的影响，图 6 表明偏差、倾角、β 与特征谐波实部的关系，其中 β 由 π/6 取到 π/6，每次变化量为 π/12，图中 β 共变化 5 次．偏差由 −3 变化取值到 3，间隔 0.5，共变化 11 次．此时焊接倾角 γ 取 π/6．

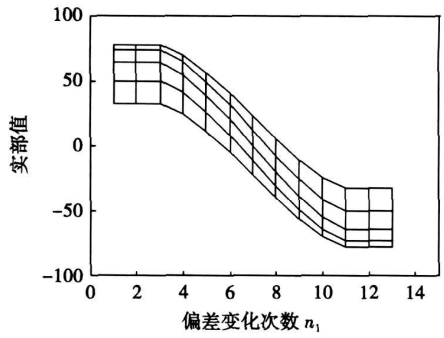

图 6　偏差、β 与特征谐波实部的关系

Fig. 6　Relationship between deviation、β change and real part of characteristic harmonic

从式(4)和图 6 都可以发现此时特征谐波实部与偏差变化的影响受到了倾角、β 的影响，但其基本线性关系不变．

3　试验结果

水淹气罩 2 cm 试验条件下，进行了 12 组焊接试验，1 ~ 4 组为完全左偏，5 ~ 8 组为对中情况，9 ~ 12 组为完全右偏．每组试验数据都包含了上千次信号采集周期．焊接参数如表 1 所示．

表 1　焊接参数

Table 1　Welding parameters

焊接电流 I/A	电弧电压 U/V	焊接速度 v/(cm·min^{-1})	干伸长 L/mm	焊炬高度 H_0/mm	气体流量 q/(L·min^{-1})	送丝速度 v_s/(m·min^{-1})	旋转频率 f/Hz
150~225	24	50	19~38	15	10~21	8~12	15

通过采集焊接电流数据，对其进行消噪处理后，采用幅值反映焊缝偏差的特征谐波检测方法，处理结果如图 7 所示．

同样一组数据，采用实部反映焊缝偏差的特征谐波检测方法，处理结果如图 8 所示．

通过图 7 和图 8 的对比结果可以发现，对中情况的 5 ~ 8 组试验中，采用实部反映焊缝偏差的特征谐波检测方法抗干扰能力更强，检测效果更好．这表明在 β 为 0 或较小时，实部法比幅角法的鲁棒性更好．

另外针对倾角变化做了 18 组试验，倾角值 γ 范围由 −40° 变化到 +40°，间隔 5° 做一组试验，相应的倾角变化数为 1 ~ 17，其余焊接参数同表 1，从图 9 中可以看出，虚部值与倾角变化也成线性关系．因此，在对数据作傅立叶变换后，可以用实部反映焊缝偏差，用虚部反映倾角变化．

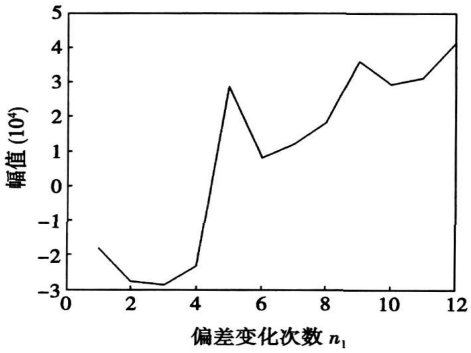

图 7 偏差变化与实际数据特征谐波幅值的关系

Fig. 7 Relationship between deviation change and amplitude of characteristic harmonic on actual data

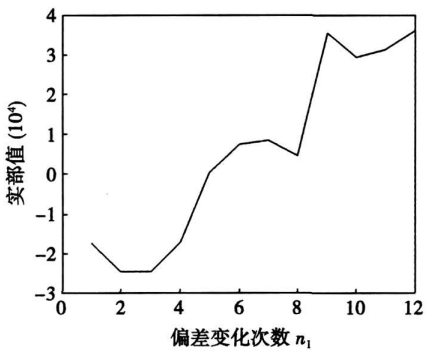

图 8 偏差变化与实际数据特征谐波实部的关系

Fig. 8 Relationship between deviation change and real part of characteristic harmonic on actual data

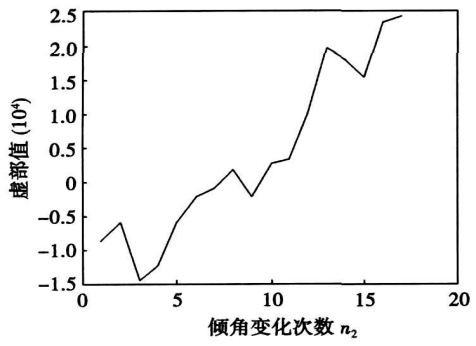

图 9 倾角变化与实际数据特征谐波虚部的关系

Fig. 9 Relationship between oblique angle and imaginary part of characteristics harmonic on actual data

采用这样的方法,就可以通过电流数据同时检测到焊缝偏差和倾角变化,并实现二者的解耦.

4 结 论

(1) 在 β 角不存在的情况下,幅角法不受倾角变化的影响,偏差与幅值基本成线性关系.

(2) 在 β 角存在的情况下,倾角绝对值越大,幅角法受倾角影响越大,其影响表现在当偏差为 0 附近时,幅值大幅偏高或偏低,造成偏差为 0 附近的判断发生很大错误.

(3) 在 β 角不存在的情况下,实部虚部法的实部与偏差成线性关系,虚部与倾角成线性关系. 受倾角变化的影响,偏差与幅值基本成线性关系.

(4) 在 β 角存在的情况下,实部虚部法的实部与偏差的线性关系受到 β 角大小的影响,β 角绝对值越大,受到的影响越大,但由于 β 角通常较小,所以所受影响比较小. 实部虚部法的虚部与偏差的线性关系也受到 β 角大小的影响,β 角绝对值越大,受到的影响越大.

(5) 在倾角和 β 同时存在的情况下,采用基于实部的特征谐波法检测偏差比基于幅角法的特征谐波法抗干扰能力更强.

参考文献:

[1] 潘际銮. 现代弧焊控制[M]. 北京:机械工业出版社,2000.

[2] 廖宝剑,吴世德,潘际銮. 电弧传感器理论模型及信息处理[J]. 焊接学报,1996,17(4):263—271.
Liao Baojian, Wu Shide, Pan Jihuan. Theoretical model and signal processing of arc sensor[J]. Transactions of the China Welding Institution, 1996, 17(4): 263—271.

[3] Kim C H, Yoo W S, Na S J. Development of an arc sensor with mechanized rotation of electrode [J]. Materials Science Forum, 2003, 426/432 (5): 4135—4140.

[4] Kim Yongjae, Sehun Rhee. Arc sensor model using multiple-regression analysis and a neural network [J]. Proceedings of the Institution of Mechanical Engineers, Part B: Journal of Engineering Manufacture, 2005, 219(6): 431—445.

[5] Narayana V L, Rao V S. Mathematical modelling of simple seam tracking process applicable in multi-function control robotic welding system [J]. Journal of the Institution of Engineers (India), 2004, 85(9): 20—26.

[6] 叶建雄. 旋转电弧传感焊枪倾角检测及水下焊缝跟踪技术研究[D]. 南昌:南昌大学,2007.

作者简介:李志刚,男,1971 年出生,博士研究生,高级工程师. 主要研究方向为焊接机器人及焊接自动化. 发表论文 6 篇.

Email: gordon7456@163.com

dong, China). p37—41

Abstract: The nanostructured ZrO_2 laser glazed coating was produced with different glazing processing parameters. Experiments were done to investigate the microstructure and properties. The investigation methods include optical and scan electron microscopy test, microhardness test and thermal shock test. In addition, the change rules of microstructure and properties were discussed. The results show that the depth, width and microhardness of the coating increase with the laser specific energy being increased. Microstructure test and thermal shock test show that the surface morphology and thermal shock resistance of the coating have relation to the laser specific energy. When the specific energy is about 37.2 J/mm^2, the laser glazed coating exhibits the best thermal shock resistance.

Key words: nanostructured ZrO_2 coating; laser glazing; specific energy; surface morphology; thermal shock resistance

Analysis on property and microstructure of Mo-Si composite coating deposited by argon shielded arc on Q235 steel surface

WANG Yongdong, LIU Xing, ZHU Yan, MAO Xinyu (Department of Material Science and Technology, Heilongjiang Institute of Science and Technology, Harbin 150022, China). p42—44

Abstract: Metal-silicide composite coating of FeMoSi/Fe_3Si was prepared by in situ synthesis on the surface of Q235 steel by means of argon arc cladding technique with the pre-alloyed powder of Mo and Si. The microstructure and phases of coating were investigated by scanning electron microscope (SEM) and X-ray diffraction (XRD), meanwhile the microhardness and the wear resistance of coating were tested. The results show that the interface between the coating and substrate has excellent bonding and is free of pores and cracks. Microstructure of the coating is mainly composed of α-Fe, primary dendrite FeMoSi and interdendritic FeMoSi/Fe_3Si eutectic structure. The microhardness was 3 times higher than that of Q235 steel and the maximum microhardness can reach 1 000 HV0.2, the wear resistance of coating was 11 times higher than that of Q235 steel substrate.

Key words: argon arc cladding; composite coating; situ synthesis; wear resistance

Influence of activating flux on undercut and fatigue property of welded joints

CHAI Guoming, ZHANG Hui (National Key Laboratory for High Energy Density Beam Processing Technology, Beijing Aeronautical Manufacturing Technology Research Institute, Beijing 100024, China). p45—48, 52

Abstract: In activating flux PAW welding, the undercut and fatigue property were studied. The results show that the increase of welding speed can improve the welding efficiency, but the undercut appears. The deposited metal in activating flux PAW welding increases, the arc force strengthens, the arc voltage is higher, the arc stiffness strengthens and the arc is much more stable, which would make the deposited metal flow to the toe zone. The deposited metal would fill up the toe zone. Compared with the specimen without activated flux, the fatigue strength of specimen with activating flux has been increased by 60% at most. The activating flux can make the undercut reduce or vanish and make the fatigue property increase.

Key words: activating flux; undercut; fatigue strength

Molecular dynamics simulation of diffusion behavior between the interface of Cu/Sn

CHENG Hongtao, YANG Jianguo, LIU Xuesong, FANG Hongyuan (State Key Laboratory of Advanced Welding Production Technology, Harbin Institute of Technology, Harbin 150001, China). p49—52

Abstract: With the molecular dynamics simulations based on modified embedded atom method (MEAM) potentials, the discussion was presented about the diffusion behavior of the interfacial reaction in the soldering wetting process, and the theoretical analysis was used to explain the soldering diffusion process on the base metal from the view of atomic scale. The simulation results indicate that, when the reaction reaches the balance state, the mean square displacement of the atoms motion varies linearly with the reaction time step, the diffusion speed of the solder atoms in x direction is equal with that in the y direction, and both are faster than that in the y direction. Based on the equation of Einstein, the diffusion coefficients of the solder atoms spread on x, y, z directions are 2.03×10^{-9}, 2.05×10^{-9}, 5.06×10^{-10} cm^2/s, respectively. The diffusion coefficient of z direction is in good agreement with the experiment value, which agrees with the macroscopic proceeding in the soldering.

Key words: wetting; interfacial diffusion; molecular dynamics; Einstein equation

Improvement of characteristic harmonic method in rotational arc sensor

LI Zhigang, ZHANG Hua, Gao Yanfeng (Institute of Mechatronics Engineering, Nanchang University, Nanchang 330031, China). p53—56

Abstract: The characteristic harmonic method was used to detect the deviation of rotating arc sensor. Through the mathematical analysis and simulation of arc length model, the relationship between the weld seam deviation, welding torch obliquity, the initial phase and the phase angle of tracking were studied. The characteristic harmonic method was improved by the conclusion that the real part and imaginary part can be used to detect the weld seam deviation and welding torch inclination, respectively. Also, in the case of only weld seam deviation is detected, the use of real part of characteristic harmonic is better than the amplitude method. The experiment results show the improved characteristic harmonic method has stronger anti-interference ability than that of the traditional characteristic harmonic method.

Key words: rotational arc sensor; deviation detection; char-

acteristic harmonic

Intelligent inspection of soldered joint based on artificial neuron network LU Shenglin[1], Zhang Xianmin[2] (1. School of Mechanical Engineering, Dongguan University of Technology, Dongguan 523106, Guangdong, China; 2. School of Mechanical Engineering, South China University of Technology, Guangzhou 510640, China). p57—60

Abstract: As electronic components get smaller and the board densities become more compact, it is necessary for automatic inspection in electronic manufacturing. The automatic optical inspection (AOI) system is demanded more precise and intelligent. The traditional inspection methods require large quantity samples of all types to train the inspector, or do some complicated setting. To overcome the disadvantages, an intelligent method was proposed. Firstly, a series of features of soldered joints were defined. Then, an automatic boundary setting method based on statistic was introduced. Finally, the neural network was established to classify the soldered joints. The performance of the method was verified by the experiment.

Key words: solder joint; neural networks; machine vision; inspection

Application of combined welding heat source in arc welding simulation GAI Dengyu[1], CHU Yuanzhao[1], LI Qingfen[2], LiLi[1] (1. Material Science and Chemical Engineering College, Harbin Engineering University, Harbin 150080, China; 2. Machinery and Electrical College, Harbin Engineering University, Harbin 150001, China). p61—64, 68

Abstract: Factors of various welding heat sources were analyzed. It is found that Gaussian heat source and double ellipsoidal heat source can not indicate welding molten pool exactly in weld simulation. The combined welding heat source which combined Gaussian face heat source with double ellipsoidal body heat source was used in welding simulation. The welding molten pool calculated with the combined welding heat source consists with practice fusion line. The temperature field and stress field of stainless steel by arc welding were simulated with these three kinds of welding heat sources. The residual stress field simulated using the combined welding heat source is in good agreement with test and more exactly than those using the other two heat sources.

Key words: simulation; combined heat source; residual stress

Microstructure and high temperature abrasion resistance of Ni-based WC composite layer deposited by plasma arc FU Wei[1], WANG Xibao[2], CHEN Guoxi[1] (1. Baosteel Machinery Plant Surface Technology Institute, The Surfacing Institute of Machinery Maintenance Ltd., Baosteel, Shanghai 201900, China; 2. School of Materials Science and Technology, Tianjin University, Tianjin 300072, China). p65—68

Abstract: The Ni-based alloy powder with 60% WC was deposited on the surface of 15CrMo by plasma arc surfacing. The microstructures, hardness and wear resistance of the layer were analyzed. The results show that the layer has good external appearance and the WC particles which maintain its high hardness and exhibit few refusion distributes uniformly across the section of the layer. The layer also has high hardness and wear-resistance at elevated temperature, which is 5 times than that of 45 normalized steel.

Key words: plasma transferred-arc; WC particle; microstructure; wear-resistance at elevated temperature

Effect of Ag and Ni on melting temperature and spreadability of Sn-Sb-Cu solder alloy FENG Lifang[1], YANG Li[2], YAN Yanfu[1], GUO Xiaoxiao[1], ZHANG Keke[1] (1. Henan Key Laboratory of Advanced Non-ferrous Metals, Henan University of Science and Technology, Luoyang 471003, Henan, China; 2. College of Electromechanical Technology, Xuzhou Institute of Technology, Xuzhou 221008, Jiangsu, China). p69—72

Abstract: In order to improve the properties of the Sn-10Sb-8Cu solder alloy, two new lead-free solders (Sn-Sb-Cu-Ag and Sn-Sb-Cu-Ni) were made by adding small amounts of Ag and Ni into Sn-10Sb-8Cu solder alloy. Results show that the melting temperatures of the Sn-Sb-Cu-Ag solder alloys decrease and the spreading areas increase compared with those of the matrix solders, which are related to the increase of the superheat degree, the dispersed distribution of SnAg phase with low melting point and the decrease of the surface tension of the melting solder. The melting temperatures of the Sn-Sb-Cu-Ni solder alloys decrease and the spreading areas of the Sn-Sb-Cu-Ni solder alloys are slightly less than those of the matrix solders. It is because the viscous and the surface tension of the Sn-Sb-Cu-Ni melting solder increase and the Cu_6Sn_5 is covered by the polyhedron-shape $(Cu, Ni)_6Sn_5$ which is adverse to the spreadability of the solder by adding small amount of Ni.

Key words: Sn-Sb-Cu alloy; lead-free solder; melting temperature; spreadability

Numerical simulation on temperature field in on-site induction brazing of tubes ZHANG Wei, QI Bojin, XU Haiying (School of Mechanical Engineering and Automation, Beijing University of Aeronautics and Astronautics, Beijing 100191, China). p73—76

Abstract: Considering the characteristics of on-site induction brazing of tubes, the FEM model was built. Based on the electromagnetic and thermal coupled finite element method, the temperature distribution on tubes was simulated by ANSYS. The results show that temperature distribution on tubes is nonuniform. Using a six-point synchronous temperature measurement system with thermocouples,